Impact of structured heterogeneities on reactive two-phase porous flow

Daniel Reeves and Daniel H. Rothman

Phys. Rev. E **86**, 031120 — Published 14 September 2012

DOI: 10.1103/PhysRevE.86.031120

Impact of structured heterogeneities on reactive two-phase porous flow

Daniel Reeves* and Daniel H. Rothman

Lorenz Center and Department of Earth,

Atmospheric, and Planetary Sciences,

Massachusetts Institute of Technology, Cambridge, MA

Abstract

Two-phase flow through heterogeneous media leads to scale-free distributions of irregularly-shaped pockets of one fluid trapped within the other. Although reactions within these fluids are often modeled at the homogeneous continuum scale, there exists no current framework for upscaling from the pore scale that accounts for the complex and scale-free geometry of the bubbles. In this paper, we apply a linear-kinetics diffusion-reaction model to characterize the steady-state chemical environment inside the irregular pockets. Using a combination of theory and invasion-percolation simulations, we derive scaling laws describing the distribution of diffusion times within bubbles. We show that chemical concentrations within the bubbles are determined by the Laplace transform of the entire distribution of diffusion times from each location. This serves as a means to compute average concentrations of reactant within a bubble of unique geometry and size. Furthermore, the overall system size imposes upper bounds on the distribution of bubble sizes, thereby imposing a system-size dependence on the statistics and average concentrations. These conclusions have profound implications for continuum models of porous reactive-flow, where kinetic and equilibrium parameters are often chosen from laboratory measurements made at centimeter scales.

PACS numbers: 82.33.-z, 64.60.ah, 91.67.Bc

*Electronic address: dreeves@mit.edu

I. INTRODUCTION

Two-phase flow in porous media induces spatial heterogeneities in the distribution of the two phases. We consider a situation in which one phase provides a reactant that diffuses into and is consumed within the other phase. Therefore, the fluid-fluid interface provides a complex boundary condition for the reaction within the second phase. The reactant could be a single reactive chemical component, such as hydrogen ions, or could be a more general parameter describing the state of a multicomponent reactive system. In either case, we assume that the variable diffuses into the reactive phase and slowly approaches a new equilibrium.

Specifically, we consider the heterogeneous geometry resulting from an invasion-percolation with trapping (IPT) model in which one fluid, the invader, partially displaces the other fluid, the defender [1–3]. The porous medium is assumed to have widely distributed pore sizes and throats, leading to a sequential filling of the pore space by the invading fluid and a retreat by the defending fluid. This process continues until all defending fluid has either exited the system or has become "trapped" as disconnected bubbles.

The application that inspires this work is the geological storage of CO_2 for purposes of carbon sequestration. At geological carbon sequestration sites, supercritical CO_2 is injected into subterranean reservoirs, thereby displacing the existing salty water, or brine. Reactive transport simulations of these reservoirs are typically performed at Darcy-scale resolutions of centimeters or meters [4, 5], over which the heterogeneities of the porous material and the emergent dynamics of the invasion process are lost. The reactions are assumed to be well-mixed within representative volume elements (REVs), and the chemical kinetic and equilibrium parameters that are utilized in the models are those obtained from laboratory measurements on well-mixed fluids or flooded cores [6, 7]. Such measurements are more appropriately applied at the micron scale of the single pore. Whether or not it's also appropriate to apply such parameters to heterogeneous systems that are coarse-grained at larger length scales is not resolved. Furthermore, percolation processes give rise to structures with length scales that follow power-laws and span many orders of magnitude. Upper cutoffs for these scaling behaviors may be larger than simulation resolutions. This challenges the very applicability of diffusive-transport models with fixed parameters. To date, there have been some efforts to upscale from pore scale to reservoir scale in these contexts [8–16], especially

regarding transport and reaction in hierarchical structures. However, there are few studies that consider the presence of similar structures at all length scales and how those structures influence overall chemical rates. A complete cohesive framework is lacking, and this work contributes to completing that framework.

In this paper, we explore how the emergent geometries of invasion percolation affect chemical reactions bounded by those geometries. We use single-component diffusion-reaction equations to focus on the complex boundary conditions and draw conclusions regarding how the geometry determines chemistry. Realistic scenarios, such as within the carbon sequestration reservoirs mentioned above, likely involve complicated multi-component chemistries [17]. In some instances, the overall dynamics of multi-component precipitation-dissolution systems can be characterized with a reduced number of variables [18, 19], and perhaps such an approach can be applied to the carbonate systems of interest. Detailed diffusion-reaction modeling of multi-component systems is important and interesting [20, 21], but is often performed with simple geometries describing the boundary conditions. We complement those studies by applying complex geometric boundary conditions to a simple reactive system.

We show that the chemistry at each point in the reactive phase is determined by the Laplace transform of the distribution of first-passage diffusion times to the fluid-fluid interface. Numerical simulations show that the distributions are similar to inverse Gaussian distributions and can be characterized with the first two moments. Distributions of these parameters follow simple power-laws. Interestingly, the functional form and the scaling exponents for the moments can be predicted using a simple circular approximation for the bubbles in two dimensions, but the corresponding spherical approximation in three dimensions fails to predict the correct scaling exponents. We find that averages such as chemical concentration, when measured over an isolated bubble, depend on both size and complex shape. Furthermore, the power-law distribution of bubble sizes implies that chemical concentrations averaged over the entire system depend upon the arbitrary choice of system size. This complication must be accounted for in any accurate coarse-graining of the system.

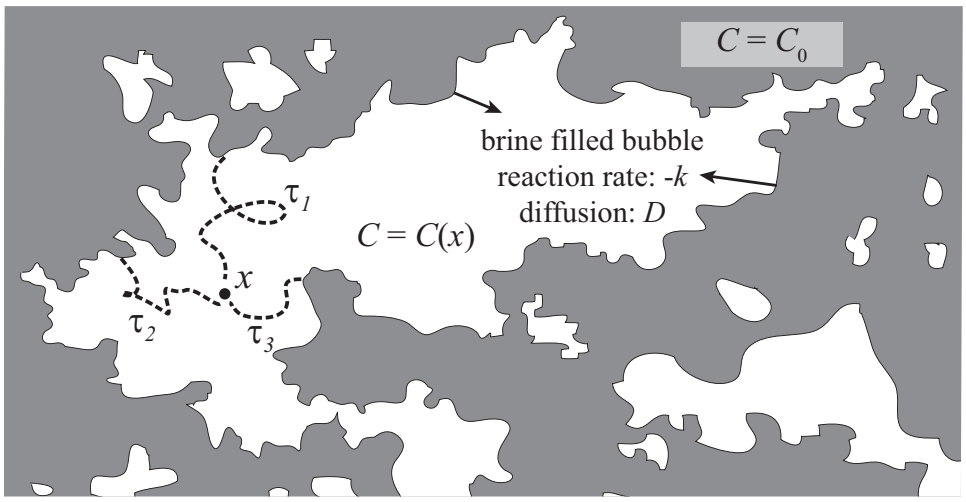

FIG. 1: The concentration of a reactant is fixed at the interface between a surrounding fluid (gray) and bubbles of the isolated fluid (white). The reactant diffuses into the isolated fluid and is removed at rate k. The resulting concentration at every location x within the isolated fluid can be described by the distribution of diffusion times, τ_i, from the boundary to x. Note that the figure represents only the fluid phases, and the porous solid phase is not shown.

II. THEORY

A. What physics and geometry control the chemistry in a heterogeneous system?

We describe the chemical state of our system at each location x with the concentration $C(x)$. Within the reactive fluid, the reactant is removed at the rate $kC(x)$, and diffuses with diffusion constant D. As mentioned above, $C(x)$ can also be considered a generic state variable that diffuses and decays to an equilibrium value within the reactive phase. The reactive fluid is surrounded by an "inert" fluid, in which the concentration is fixed at C_0 (see Fig. 1). The interface Γ therefore supplies the boundary condition $C(\Gamma, t) = C_0$, for the diffusion-reaction equation,

$$\frac{\partial C(x,t)}{\partial t} = D\nabla^2 C(x,t) - kC(x,t). \tag{1}$$

We are interested in results at steady-state, where $\frac{\partial C(x,t)}{\partial t} = 0$.

We use the invasion percolation with trapping (IPT) model as the generator of the geometry (Fig. 2). IPT is a quasi-static model of two-phase flow through porous media first proposed by Wilkinson and Willemson [1]. It accounts for the heterogeneities in pore body

and throat sizes by assigning a preference number to each. The pore space is then occupied sequentially by the "invading" fluid via the highest preference pore contiguous to the previously occupied cluster. In bond percolation, the preference represents the dependence on throat size in the capillary pressure necessary to enter pores within a medium. If the invading fluid is non-wetting and the previously resident, or "defending" fluid wetting (relative to the surface), then the widest adjacent throat presents the lowest pressure barrier. The driving force increases the pressure in the connected invading cluster until it reaches that lowest barrier, and then the fluid pops through the throat into the adjacent pore, simultaneously releasing the pressure. The pressure again increases, and the process repeats.

If a cluster of the defending fluid becomes disconnected from the outside reservoir and surrounded by the invading fluid, then the defending cluster is trapped and frozen, and no more invasion can occur within that cluster. In our application, the trapped bubbles of defending fluid constitute the reactive phase, and the concentration of reactant is fixed within the invading phase.

We should note that there are limitations to the invasion percolation model of two-phase porous flow. Several mechanisms and details are omitted, such as thin films of the wetting phase coating the pore walls [22], bubble formation via "pinch-off" [23], and changes in bubble shape due to evaporation. The implications of these simplifications will depend upon the application, such as the injection of super-critical carbon dioxide into reservoirs. Before applying the details of the theory to a given application, the limitations must be carefully considered.

We construct L^2 and L^3 matrices of initially vacant pores. We begin by assigning random values to all bonds and occupying the center pore. At each time step, we find the lowest numbered bond contiguous to the occupied cluster and occupy the adjacent pore, provided that pore is not part of a disconnected bubble. The edges of the system are considered open, in that they always provide an egress for defending fluid. The process is continued until all pores are occupied or part of disconnected bubbles.

The results and conclusions of this paper do not hinge upon our choice of percolation model. Although we recognize IPT as a decent approximation of the $scCO_2$ invasion process of interest, we use it primarily as an algorithm to generate heterogeneous, multi-scale, geometries. These geometries may alternatively be due to heterogeneous pore structures, fractures [24], rock compositions, or other invasive flow models.

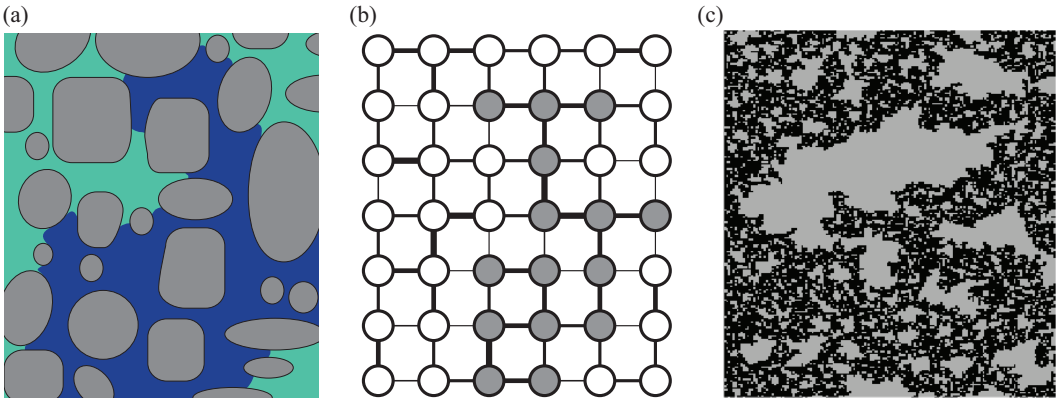

FIG. 2: (Color online) Schematic representation of bond invasion percolation. (*a*) As a non-wetting fluid displaces a wetting fluid, pores are preferentially invaded via the largest connecting throats. (*b*) Sites on a lattice are occupied sequentially via highest valued bonds, indicated by the thickest lines. (*c*) A portion of one 1000x1000 lattice, where disconnected bubbles of defending fluid are shown in gray.

B. Chemistry is determined by distributions of first passage times

In general, the steady-state concentration everywhere within the reactive phase is determined by Eq. (1) and the boundary geometry determined by the percolation mechanism. However, those exact solutions require numerical approaches that have two shortcomings. First, numerical solutions by themselves would yield few insights into and little understanding of the scaling behavior of the system. We would like to understand the physical and geometric characteristics of the interface that control the chemistry. Second, the discrete lattice geometry presents sharp edges that can be troublesome in numerical solutions. Interpreting results at the required sub-lattice resolution would not be straightforward.

Instead, we take an approach that yields insight and is appropriate on discrete lattices. We can express the reaction-diffusion equation Eq. (1) with the following:

$$\frac{dC(x,t)}{dt} = D\nabla^2 C(x,t) - \frac{k}{N}\sum_{i}^{N} C_i(x,t), \tag{2}$$

where we express the concentration at x as a superposition of the many colocalized parcels of fluid, $C(x,t) = \sum_i C_i(x,t)$. Each parcel departs the boundary carrying a concentration of $C_i(\Gamma, 0) = C_0$. It then diffuses through the bubble and reacts independently of all other parcels. The linearity of the kinetics allows us to write the total chemical reaction rate at

each x as a superposition of the reactions of the colocalized parcels. The concentration for a parcel of age τ is described by

$$C_i(\tau) = C_0 e^{-k\tau}, \tag{3}$$

where τ is the time since the parcel left the boundary. We now write that the total concentration at x is the sum over the exponential decays:

$$\frac{C(x,t)}{C_0} = \sum_i e^{-k\tau_i} = \int_0^\infty P_t(\tau, x) e^{-k\tau} d\tau, \tag{4}$$

where $P_t(\tau, x)$ is the distribution of ages, τ, of the parcels found at x at time t ($\tau < t$). At steady state, all ages are represented, $t \to \infty$, and P_t becomes the full distribution $P(\tau, x)$ of first-passage times (FPTs) for diffusion from the bubble boundary to the location x. We note that Eq. (4) is equivalent to the Laplace transform of the distribution of diffusion times.

Furthermore, we find that the mean first-passage time is insufficient to describe the evolution of the concentrations. If $\langle\tau\rangle$ were to describe the system, we would have that

$$C_{\text{mfpt}}(x) = C_0 e^{-k\langle\tau\rangle}. \tag{5}$$

We compare this incorrect result to the correct expression for $C(x)$, which is the mean of the exponential [25]:

$$C(x) = C_0 \langle e^{-k\tau} \rangle. \tag{6}$$

It follows that any scalar, such as an "effective diffusion length" does not accurately predict the chemistry. The full distribution of diffusion times is necessary.

If the reactions are non-linear, then we cannot express the reaction-diffusion system as a sum over independent parcels. The parcels mix in that the reaction of parcel i at location x depends on the evolution of all other colocalized parcels concurrently at x. In that case, the distribution of diffusion times is in general insufficient to accurately predict the chemistry. However, the scaling forms and qualitative lessons learned from our analysis are likely still relevant.

C. Analytic approximation of bubbles as discs and spheres

Our goal is to characterize the chemical concentration, $C(x)$, everywhere in the whole system. To that end, Eq. (4) instructs us to compute the distribution of first-passage times

to the interface from each location within the bubbles that emerge from the percolation process. We have separated the chemistry from a purely geometric problem. To find analytic solutions, we first approximate the complex shaped bubbles as discs in two dimensions and as spheres in three dimensions. We hypothesize this may be a reasonable approximation because the interior of the bubbles, where the diffusive process takes place, is Euclidean like a simple sphere in that the volume scales as $M(R) \sim R^d$, where R is the linear dimension of the bubble and d is the Euclidean spatial dimension. The perimeters of the bubbles are fractal [26–28] and diffusive processes on fractal surfaces have anomalous characteristics [29]. However invasion percolation with trapping (IPT) prohibits the formation of bubbles within bubbles. This prohibition ensures that the interior is Euclidean, and therefore the anomalous characteristics of fractal diffusion do not apply to diffusion within the bubble.

In this section, we solve distributions of first-passage times out of discs and spheres and compute the first two moments of those distributions. We then find scaling relationships for the distributions of those moments given an ensemble of spheres. We distribute the disc and sphere sizes identically to bubble sizes produced by percolation processes:

$$P(M) \propto M^{-\epsilon}, \tag{7}$$

where $\epsilon \approx 2.05$ (2.17) in two (three) dimensions [2]. In this way, we develop an analytic approximation for the distribution of functions $P(\tau)$ in the system, and thus, the distribution of $C(x)$.

1. *Analysis for two-dimensional discs*

For a single disc of radius R, the distribution of first-passage times can be found using the Green's function for diffusion of a particle originating a distance r_0 from the center and vanishing at the boundary. The Green's function, $C(r, \theta, t; r_0)$, is equivalently the concentration at (r, θ) and time t of particles originating at $(r_0, 0)$. $C(r, \theta, t; r_0)$ can be expressed as a series of Bessel functions [30],

$$C(r, \theta, t; r_0) = \frac{1}{\pi R^2} \sum_{n=-\infty}^{\infty} \cos(n\theta) \sum_{q_i} e^{-Dq_i^2 t} \frac{J_n(q_i r) J_n(q_i r_0)}{[J_n'(qR)]^2}, \tag{8}$$

where D is the diffusion constant and J_n are Bessel functions of the first kind. The q_i are the roots of $J_n(Rq_i)$. The distribution of first-passage times is equivalent to the total flux

of walkers absorbed at the perimeter:

$$P(\tau, r_0) = \int_0^{2\pi} \mathrm{d}\theta \, RD \left. \frac{\mathrm{d}C(r, \theta, \tau; r_0)}{\mathrm{d}r} \right|_{r=R}, \tag{9}$$

which gives another sum of Bessel functions. Simplification yields

$$P(\tau, r_0) = \frac{2D}{R} \sum_{q_i} e^{-Dq_i^2 \tau} q_i \frac{J_o(q_i r_0)}{J_1(q_i R)}. \tag{10}$$

We evaluate this series numerically for many parameter values and note that the distributions, $P(\tau)$, appear to be well approximated by inverse Gaussian distributions (see Fig. 3),

$$P_{IG}(\tau) = \left(\frac{\lambda}{2\pi\tau^3} \right)^{1/2} \exp \frac{-\lambda(\tau - \mu)^2}{2\mu^2 \tau}. \tag{11}$$

This is expected because the distribution of FPTs to absorbing walls enclosing a finite interval in one-dimension is given by a sum of inverse Gaussians. Next, we compute the mean and variance of the first-passage time, $\mu(r_0, R) = \langle \tau \rangle$ and $v(r_0, R) = \langle (\tau - \mu)^2 \rangle$ using Eq. (10). They are given by

$$\begin{aligned} \mu(r_0, R) =& A(R^2 - r_0^2) \\ v(r_0, R) =& B(R^4 - r_0^4), \end{aligned} \tag{12}$$

where $A = 0.5$ and $B = 0.125$. The characteristic length scale in the percolation geometry is prescribed by the size of one pore, or one lattice unit, of length a. Therefore, the choice of diffusion constant is arbitrary and fixes a characteristic diffusion time, $a^2/2D$. We fix $D = a^2/2 = 1/2$ so the diffusion time between individual pores is equivalent to a step of duration unity in a discrete random walk [31]. In Section IV B, we compare the arbitrarily scaled diffusion times with reaction rate constants presented in the same units.

Equation (12) characterizes the first-passage times from a single location within a disc to the edge of the bubble. A finite system of bubbles therefore carries a distribution of means and variances determined by both the distribution of sphere sizes and the distribution of distances within a single disc. If $P(\mu, v)$ is the total density of these moments across the system, then because each area or volume element can be characterized by either μ and v or by r and R, we can write

$$\iint \mathrm{d}\mu \, \mathrm{d}v \, P(\mu, v) = \frac{1}{V} \int_a^{R_{\max}} \mathrm{d}R \int_0^R \mathrm{d}r \, N(R) Q(r|R) \tag{13}$$

where V is the total area or volume of the system, $N(R)$ is the number density of discs of radius R in the system and $Q(r|R)\,\mathrm{d}r$ is the area within a disc of size R that is between distances r and $r + \mathrm{d}r$ from the center. The lower limit on R exists because no bubbles are smaller than a single pore and the upper limit represents the largest bubble size allowed by the finite system size (or additional physics discussed in Section IV B 5).

To use Eq. (13) to derive the distribution of time variables from geometric variables, we first find distributions of the geometric properties of discs. Adopting the scaling for our bubbles given in Eq. (7), we apply the relationship $M = \pi R^2$ to find the corresponding number density of discs with radius R:

$$N(R) = CR^{-\beta}, \tag{14}$$

where $\beta = 2\epsilon - 1 \approx 3.11$. Applying our limits on R, the normalization prefactor is $C = (\beta - 1)/(a^{(1-\beta)} - R_{\max}^{(1-\beta)})$. The conditional area density per disc $Q(r|R)$ is simply $2\pi r\Theta(R - r, r, R - a)$, where the step function $\Theta(x_i) = 1$ if all arguments $x_i > 0$. This ensures $r < R$, $r > 0$, and $R > a$.

Using Eq. (12) we rewrite the product of the differential lengths using the Jacobian,

$$J = \frac{\partial\mu}{\partial R}\frac{\partial v}{\partial r} - \frac{\partial\mu}{\partial r}\frac{\partial v}{\partial R} \tag{15}$$

$$= 8ABRr(R^2 - r^2). \tag{16}$$

We find the density of the two time parameters,

$$P(\mu, v) = \frac{N(R)Q(r|R)}{VJ} \tag{17}$$

$$= \frac{\pi C}{4VAB}\frac{R^{-(\beta+1)}}{(R^2 - r^2)}\Theta(R - r, r, R - a). \tag{18}$$

Substituting for R and r with μ and v, we find

$$P(\mu, v) = \frac{2^{(\beta-3)/2}C\pi}{VB\mu}\left(\frac{Av}{B\mu} + \frac{\mu}{A}\right)^{\left(-\frac{\beta+1}{2}\right)}\Theta\left(v - \frac{B\mu^2}{A^2}, v + \frac{B\mu^2}{A^2} - 2Ba^2\right). \tag{19}$$

This gives the distribution of means and variances of first-passage times from interior locations to interfaces across an ensemble of discs. The integrated distribution of means for an infinite system with negligible a is

$$P(\mu) = \int_0^\infty P(\mu, v)dv \propto \mu^{-(\beta-1)/2} = \mu^{-1.055} \tag{20}$$

Similarly, the distribution of variances is

$$P(v) = \int_0^\infty P(\mu, v) d\mu \propto v^{-(1+\beta)/4} = v^{-1.028} \tag{21}$$

In a finite system, the limits a and $R_{\max}$ provide bounds on the above scaling behavior; the scaling is valid for means and variances larger than those associated with discs of size a.

2. Analysis for three-dimensional spheres

In three dimensions, we apply an identical analysis, albeit with slightly modified distributions. First, instead of analytically finding the Green's function for diffusion in spheres, we directly simulate random walks in a sphere to compute distributions of first passage times from starting locations to the boundary. Although Eq. 12 was initially derived in 2D using Green's functions, the results of the 3D simulations are consistent with the form of this equation. Therefore, we adopt Eq. 12 as an empirical description of the 3D behavior, with constants $A = 0.33$ and $B = 0.045$.

In the three dimensional case, we apply the appropriate relationships $M = 4\pi R^3/3$ to Eqs. 7 and 14. This yields $\beta = 3\epsilon - 2 \approx 4.5$. The conditional volume per sphere is now $Q(r|R) = \pi r^2 \Theta(R - r, r, R - a)$. We use Eq. 17 to find the density of the time parameters to be

$$P(\mu, v) = \frac{\pi C}{2VAB} \frac{rR^{-(\beta+1)}}{(R^2 - r^2)} \Theta(R - r, r, R - a) \tag{22}$$

$$= \frac{2^{(\beta-3)/2} C\pi}{VB\mu} \left(\frac{Av}{B\mu} + \frac{\mu}{A} \right)^{\left(-\frac{\beta+1}{2}\right)} \Theta\left(v - \frac{B\mu^2}{A^2}, v + \frac{B\mu^2}{A^2} - 2Ba^2 \right). \tag{23}$$

The overall distribution of means and variances can again be found in three dimensions by integrating over m and v:

$$P(\mu) \propto \mu^{-(\beta/2-1)} = \mu^{-1.25}, \tag{24}$$

$$P(v) \propto v^{-(\beta/4)} = v^{-1.125}. \tag{25}$$

From this analysis, we form several predictions for the distributions of first-passage times measured on the geometry formed by IPT. First, the distributions from single locations can be approximated by inverse Gaussian distributions, which can be characterized solely by the mean and variance. The bivariate histogram of the means and variances will resemble

Eq. (23). It will exhibit high density along $v = \mu^2$ and no density below that line. Furthermore, the collapsed histograms of the means and variances will follow power-law scaling with exponents given above.

III. FIRST-PASSAGE TIME DISTRIBUTIONS

A. Distribution of FPTs out of percolation bubbles

Distributions of first-passage times are measured by simulating random walks originating at each location within the bubbles, and terminating at the fluid-fluid interface. To ensure that first-passage time distributions for short excursions (about one step) match exact theoretical diffusion results, the duration of each step is taken from an inverse Gaussian distribution with a mean step time along each dimension of unity (corresponding to $D = 0.5$). Over many steps, the central limit theorem ensures that the mean squared displacement scales linearly with step number, like any diffusive process. Several thousand walks are simulated originating at each location, and the total duration of the walks are recorded. Each realization of the IPT process therefore produces an ensemble of first-passage time distributions, one ensemble corresponding to each lattice site occupied by defending fluid.

Figure 3 shows distributions for three example locations. The top plot shows a computed probability density function (PDF) for a location on a cubic lattice, whereas the middle and bottom show data for locations on a square lattice. The comments in Sec. II C motivate us to compare these curves to two-parameter fits of inverse Gaussian distributions, which are given by broken lines in Fig. 3. Because of the similarity, we characterize the distribution at each location using two fitting parameters, the mean μ and variance v. The fitting procedure yields reliable measurements that are not skewed by limited data and the discrete nature of the walk.

B. Characterizing the FPTs for an ensemble of bubbles

The two fitting parameters μ and v are computed for every location occupied by residual defending fluid. Figure 4 gives bivariate histograms of those parameters collected over several lattices in both two and three dimensions. There are three main features of these histograms that are predicted by the theory of Section II C. First, the highest density lies

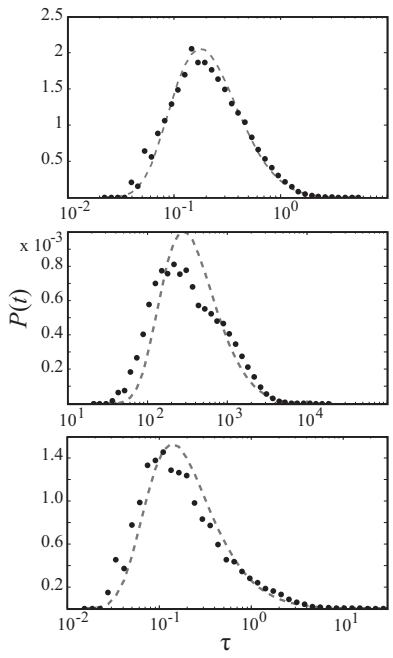

FIG. 3: Probability densities of first-passage times for diffusion to the fluid-fluid interface originating at three example locations. The process is in (*top*) three dimensions, and in two dimensions with the origin (*middle*) near the core of the bubble or (*bottom*) near the edge of a bubble. The dots represent PDFs computed from binned data, and the broken line represents a two parameter fit to an inverse Gaussian function. Note the shortness of trips in three-dimensions compared to those in two-dimensions. The units are such that the mean step time is one.

along a line $v \propto \mu^2$. Second, below the line $v = \mu^2$, there is very little density, and indeed the approximate theory predicts zero density in that region. Third, there is no density above an upper cutoff determined by the size of the largest bubbles produced on the finite lattice. This upper cutoff increases with lattice size. The limited range of μ and v in three dimensions is due to both the steep descent in the probability compounded with computational limitations on L.

We next compare the scaling behaviors predicted by Eqs. 20-25 to numerical results. Figure 5 gives histograms of μ and v integrated over several systems. The lattice sizes are $L = 2000$ and $L = 200$, in two and three dimensions, respectively. The dashed lines show predicted power-law scaling, which we expect to be valid for $\mu > A$ and $v > B$ because in simulation the lower cutoff is $a = 1$. We find that the 2D results are in excellent agreement with the circular bubble approximation, but in 3D, the agreement is very poor. Despite the

small range of values for μ, we clearly observe a more negative exponent than predicted; long-duration walks are not observed as frequently as expected. Due to the lower cutoff in bubble size, we expect the scaling laws to over-predict the prevalence of small means and variances; this expectation is opposite the observed discrepancy.

IV. DISCUSSION

A. Spherical bubble approximation: why does it fail in three dimensions?

Figure 5 demonstrates that the analytic model presented above is in agreement with numerical data in two dimensions. However, the scaling exponents in three dimensions disagree. Approximating bubbles as solid spheres overestimates the distribution of long-duration walks and underestimates the dominance of short-duration walks. In this section, we discuss differences between two and three dimensions that may explain this result, and discuss the role of the connectivity of the three-dimensional lattice. We suggest that the failure of the approximation in three dimensions is due to the stratification and filamentation of 3D clusters, which is visualized in Fig. 6. Compare the hole-filled and filamentous nature of that cluster to the 2D clusters depicted in Fig. 2.

To quantitatively compare clusters in two and three dimensions we use two measures. First, we measure the ratio of interfacial surface area to cluster volume. Figure 7 gives that ratio as a function of bubble size. In two dimensions, as the bubble increases in volume, the ratio decreases as a power of the cluster size. For a Euclidean geometric shape, like a disc, the perimeter increases linearly with linear size whereas the volume increases with the square. Therefore, such shapes would exhibit a ratio of [area]/[volume] $\sim$ [volume]$^{-1/2}$. Our observed exponent is smaller, indicating that although the volume is Euclidean, the perimeter is fractal. In three dimensions, however, we do not observe a power-law scaling. Instead, the ratio rapidly asymptotes. This behavior is expected for filamentous shapes that lack a solid core, shapes peppered with holes, and shapes with surfaces that roughen as they grow.

Our second measure is the Euler characteristic [32]. This is a topological invariant, a number that describes the shape of the cluster regardless of how it may be bent or twisted. It is classically defined for polyhedra as $\psi = V - E + F$, where V is the number of vertices,

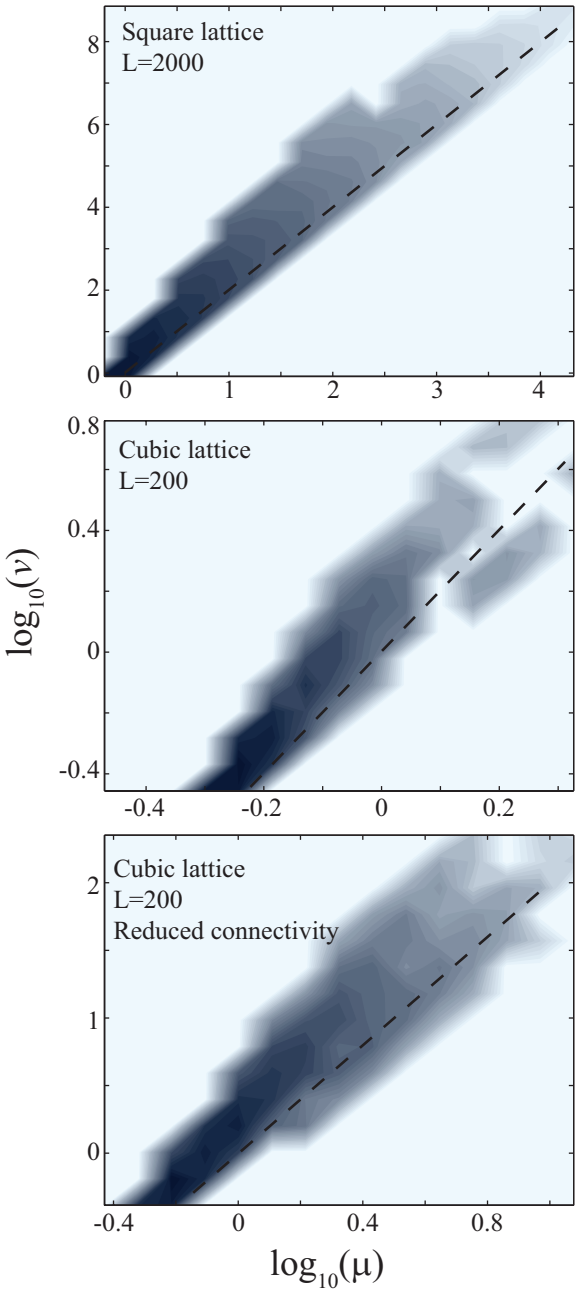

FIG. 4: (Color online) Bivariate histograms of $\log_{10}(\mu)$ and $\log_{10}(v)$ over several lattice realizations in two (*top*) and three (*middle*) dimensions, and with a reduced coordination number (*bottom*). The lattice size is $L = 2000$ in 2D and $L = 200$ in 3D. The broken line gives $v = \mu^2$. The upper cutoffs are determined by the finite lattice size.

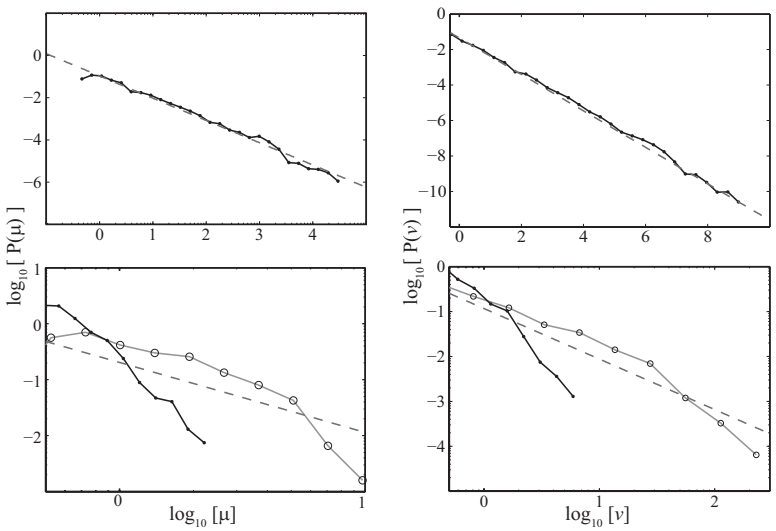

FIG. 5: Probability density of μ (*left*) and v (*right*), the mean and variance of τ. They are given for both two and three dimensions (*top* and *bottom*, respectively). The plots give both measured histograms (*solid*) and predicted scalings (*broken*) for circular and spherical bubbles. Also given are measured results for lattices with reduced coordination number (*open circles*). Despite the limited range of μ in three dimensions, we note the improved agreement with theory upon reducing lattice connectivity.

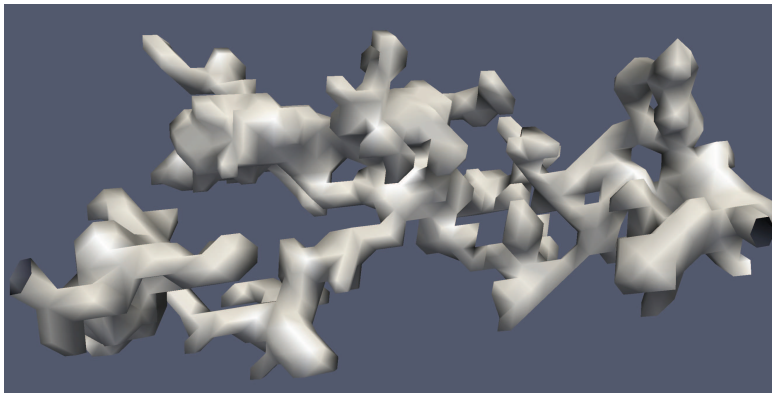

FIG. 6: (Color online) A small connected defending cluster in three dimensions. Note the filamentous and tortuous nature of the cluster.

E is the number of edges, and F is the number of faces. The Euler characteristic, ψ, of all convex polyhedra is exactly 2. For tori with n holes, $\psi = 2 - 2n$. For some non-convex polyhedra, specifically where there are pinching points where multiple faces share an edge, $\psi < 2$.

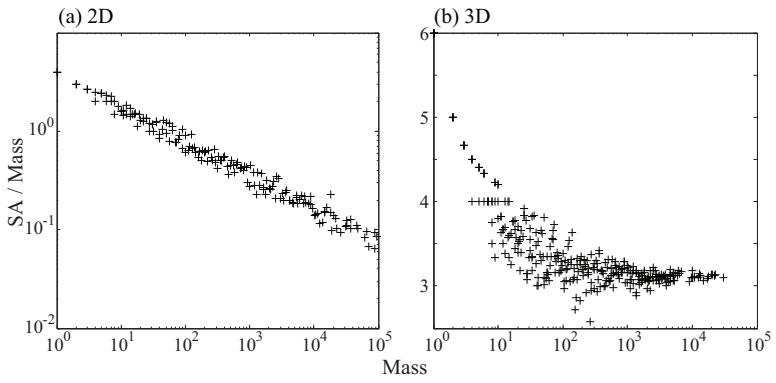

FIG. 7: Fluid-fluid interfacial surface area to volume ratio. The ratio is computed for defending bubbles in (a) two dimensions for $L = 2000$ and in (b) three dimensions for $L = 200$, and plotted as a function of bubble volume.

We measure ψ for the 3D clusters and find that the largest clusters, representing 20% of the total mass, have an average Euler characteristic of $\psi < -300$. Therefore, the clusters that we expect to contribute the largest values of μ are riddled with holes and convoluted topologies. These features bring the interior of the bubble closer to the surrounding fluid, reducing the first-passage times appreciably.

The holes and infiltrations of invading fluid into the bubbles of defending fluid lead to short diffusion times between the bubble interior and the interface. However, on latices with smaller coordination numbers (lower connectivity), this effect may be ameliorated. The cubic lattices have coordination number 6. It has been shown that for small coordination numbers ($z < 5$), the critical behavior of IPT is very different from regular percolation [33]. Specifically, the differences favor trapping. As trapping becomes more likely, we hypothesize that the bubbles develop solid cores and become less infiltrated with invading fluid thereby increasing the diffusion times from the bubble interior to the interfaces.

We test this hypothesis by excluding fluid from a random subset of lattice points when generating the bubble geometry. We exclude 30% of the sites, so the remaining accessible lattice sites have a mean coordination number 4.2. We then perform the IPT and random walk algorithms as before, where the excluded sites are off-limits to both invading fluid and random walkers.

The resulting bubbles are less filamentous and more compact. We measure the Euler characteristic (while including the excluded volume in the connected cluster) and find an

average ψ of ≈ -180 for the largest clusters, significantly higher than for unmodified lattices. We find that the surface area to volume ratios have asymptotic behaviors similar to before, but the ratios approach one, considerably lower. In these ways, the bubbles formed on the modified lattice are more solid and less stratified as those formed on the unmodified lattice, but have the same scaling features. However, the data in Fig. 5 show that bubbles formed on the modified lattice gives scalings of μ and v that are in closer agreement with the predictions for spheres. Lowering the coordination number from 6 to 4 increases the compactness of the clusters, but the behavior is still distinct from that of spheres.

B. Characterizing the overall chemistry

In this section, we describe how the overall chemistry of the system depends on the size, dimensionality, and coordination number of the underlying lattice. We discuss the physical characteristics that determine the chemistry and explore the implications for upscaling procedures. First, we determine a measurement that describes the overall system. The average chemical concentration, $\langle C \rangle$, is the natural choice. However, in many cases we are interested only in those locations that deviate substantially from the average. For example, if $C(x)$ is related to alkalinity (or generally the ability of the chemical system to neutralize acids) we may want to know how much of the system is sufficiently alkaline for a particular reaction (e.g. precipitation) to occur. Whereas the average concentration may predict that the reaction of interest occurs nowhere, the locations that deviate from the mean react differently. In general, we compute the full distribution of $C(x)$, but here we focus on and report the fraction, F, of the defending fluid for which the concentration is below a chosen threshold, C_{crit}.

We measure $\langle C \rangle$ and F over the residual bubbles as generated by the invasion percolation algorithm. This is repeated for several lattices in both two and three dimensions and the results are collated in Fig. 8. We compare the results against the predictions of our analytic spherical bubble approximations using Eqs. 4, 11, and 23. For each system size, an upper cutoff on μ is applied that is consistent with simulation. In three dimensions, the theoretical result is also compared to simulations on latices with reduced coordination number.

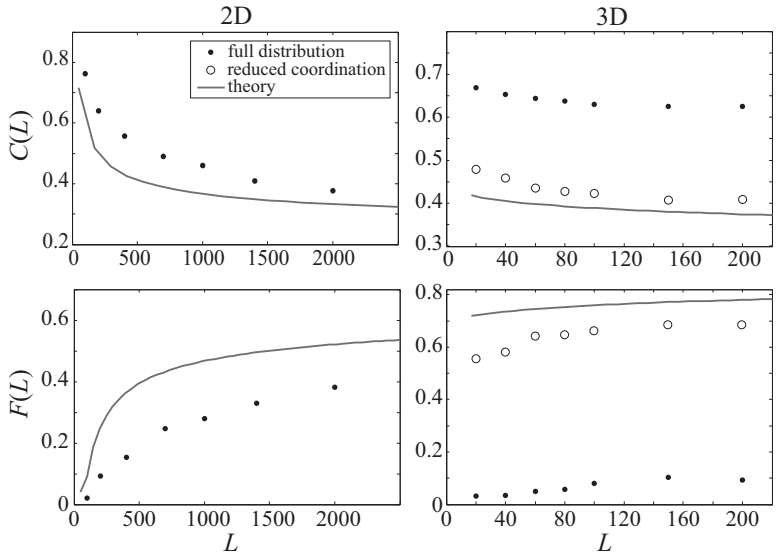

FIG. 8: Mean concentrations C (*top*) and fraction of defending fluid below threshold, F (*bottom*), as functions of lattice size, L. Results are given for both two and three dimensions. Results using the full distributions of first-passage times (*circles*) differ from those using only the mean time (*stars*). In three dimensions, results from a lattice with reduced connectivity (*open circles*) are in better agreement with theory (*line*).

1. *Chemistry depends on full distribution of first-passage times*

Our first conclusion, drawn from theory and the simulation results, is that the local and average concentrations depend on the complete distributions of first-passage times as evaluated at each point within the defending phase. A first naive approximation to computing $\langle C \rangle$ is to compute a single diffusion time averaged over the whole system and applying it to an exponential decay. This approach incorrectly accounts for the heterogeneous distribution of locations, some of which are close to interfaces and some of which are far. The next level of complexity uses mean first-passage times computed for each location, $\langle \tau \rangle$. However, we have argued that this is also insufficient and the full distribution of diffusion times from each x is necessary. Even for the simplest shaped bubbles, such as discs, the naive use of a single parameter such as a "characteristic diffusion length" to describe the local geometry at each point will inaccurately predict concentrations. Figure 9 shows the fractional error, $\Delta C = (C - C_{\rm mfpt})$, introduced by applying the mean first-passage times $\langle \tau \rangle$ in computing $\langle C(x) \rangle$ (Eq. 5) rather than applying complete distributions of first-passage times, $P(\tau, x)$

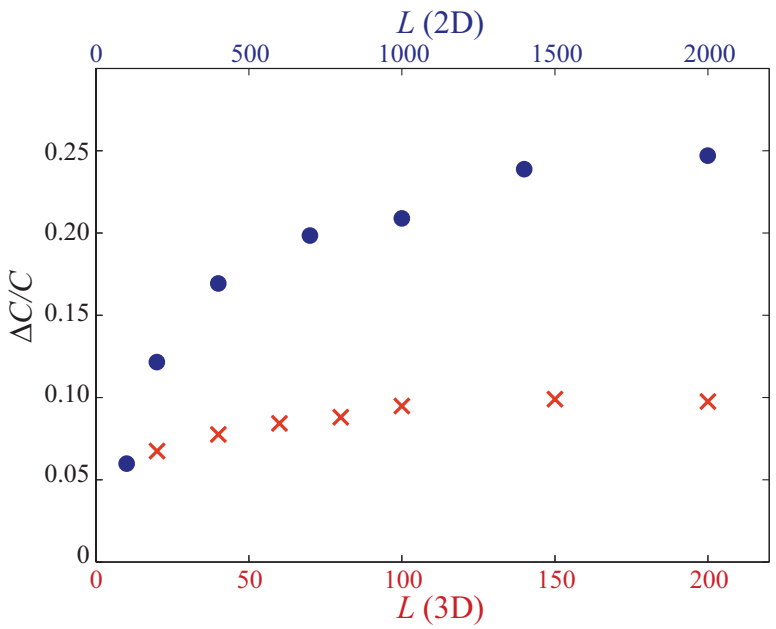

FIG. 9: (Color online) Fractional error $\Delta C/C$ introduced by applying mean first-passage times in computing $C(x)$, rather than applying the complete distribution. $\Delta C(L)/C$ is given as a function of L for both two (*dots*) and three (*crosses*) dimensions.

(Eq. 6). We see that $\Delta C(L)/C$ increases with system size, approaching 25% and 10% in two and three dimensions, respectively. In other words, the concentration at a given location is incorrectly estimated using the mean first-passage time via Eq. 5. Furthermore, although the full distribution of first-passage times is necessary to accurately describe the connection between geometry and chemistry at each location, we have found that a two-parameter description (mean and variance) offer a decent approximation.

2. Structural model of material is critical

We find that the structural model of the porous medium, and the structure of the resulting bubbles, is critical in predicting the distribution of first-passage times and resulting concentrations. Most notably, a spherical approximation for bubbles works well in two-dimensional media, but fails in three dimensions. The scaling behavior not only depends upon the dimensionality of the lattice, but also on the connectivity. This conclusion equally applies to distributions of chemical concentrations. However, the particulars of the medium and the model of bubble formation do not affect the qualitative conclusions discussed in this

Section. Equation (4) applies to all linear-kinetics models, and any correlated infiltration process will give rise to system size dependence (as discussed below).

3. Average chemistry depends on size scales

The average chemical concentration computed over a single bubble depends on the size of the bubble. As bubbles increase in size, more volume is added in the core with long diffusion times. Therefore, larger bubbles have lower average concentrations. In two-dimensions, the scaling of diffusion times as the bubble grows in volume is equivalent to that of a circle. However, in three dimensions, the scaling differs from a sphere.

When averaged over the entire system of bubbles, $\langle C \rangle$ and F depend upon the choice of system size. Bubbles exist in all sizes and are described by power-law distributions, the upper cutoff of which is determined by the size of the lattice, L. Therefore, larger lattices will generate disproportionately more numerous large bubbles, which in turn yield longer diffusion times. The average over the lattice of a quantity such as concentration will depend on L, as shown in Fig. 8, regardless of whether the quantity is experimentally measured, numerically computed, or analytically derived.

Another implication is that a given system is not equivalent to a similarly sized subdivision of a larger system. For example, an IPT realization on a 2D lattice of width L/N does not exhibit the same statistics as a realization on a lattice of size L subdivided into N^2 equal parts. First of all, a measurement averaged over the subdivisions is equal to that measured over the large lattice, whereas the smaller realizations have different statistics. Second, there is great variability and heterogeneity among the many subdivisions of size L/N. There does not exist a crossover length, λ, above which the variability among subdivisions smooths out and they exhibit equivalent statistics. However, separate IPT realizations on lattices of size L/N (not subdivisions of a realization of size L) *will* produce equivalent statistics.

4. Implications for upscaling procedures

For a very large system the scaling laws that emerge from the IPT process have lengthscale cutoffs determined by physical scaling cutoffs (discussed in the next section). Coarse graining is typically executed using well-mixed representative volume elements (REV) that are smaller

than those upper bounds. A simple approach to coarse graining is to assign kinetic and equilibrium chemical parameters that are derived from and applicable to samples of the REV size. For example, if we take laboratory measurements of dissolution kinetics in a sample of size 10 cm, then we apply those parameters to a large-scale simulation with resolution of 10 cm. However, we have shown that those measurements will vary with the size of that sample. A proper coarse-graining cannot depend on the resolution.

In an upscaling application, the applied averages must therefore be measured over the entire physical system or over a length scale determined by physical percolation. We can assign to the small REVs kinetic and equilibrium chemical parameters drawn from distributions like those measured at the largest physical length scales. Furthermore, the parameters will be highly spatially correlated because bubbles and structures span multiple REVs. Accurate upscaling procedures must capture the important correlations and heterogeneities by including variations and correlations in the parameters. An exploration of those correlations and how they can be incorporated into a coarse-graining process are topics of future work.

5. Upper lengthscales in invasion percolation

The physics of the invasion percolation process determine upper cutoffs of the emergent length scales. These are due to several forces, most notably those of viscosity and buoyancy [26, 34, 35]. At each time step, the invasion percolation process chooses for invasion the neighboring pore requiring the smallest interfacial pressure,

$$\Delta p_{\text{int}} \sim \gamma / a, \tag{26}$$

where γ is the interfacial surface tension between phases and a is the throat size. The sequential process assumes that other sources of pressure are irrelevant across the system. However, the invading fluid also experiences pressure gradients due to buoyancy and viscosity. Across a length scale $\bar{L}$, these two pressures vary by

$$\begin{aligned} \Delta p_{\text{grav}} &\sim \Delta\rho \, g \bar{L} \\ \Delta p_{\text{visc}} &\sim \frac{\mu_{\text{inv}} V \bar{L}}{\kappa}, \end{aligned} \tag{27}$$

where $\Delta\rho$ is the difference in densities between fluids, g is gravity, μ_{inv} is the dynamic viscosity of the invading fluid, V is the velocity of invasion, and κ is the absolute permeability

[34]. Above the critical buoyant and capillary length scales, the buoyant and viscous forces are greater than the interfacial forces. Therefore, across distances greater than $\bar{L}_{\rm grav}$ and $\bar{L}_{\rm cap}$, the invasion process is no longer dominated by the interfacial pressure drops across pore throats, but rather by gravitational and capillary forces. Setting Eq. 26 equal to Eq. 27, we solve for those two length scales. The dimensionless cutoffs, $L_{\rm grav} = \bar{L}_{\rm grav}/a$ and $L_{\rm cap} = \bar{L}_{\rm cap}/a$, are

$$L_{\rm grav} = \frac{1}{B_o} \tag{28}$$

$$L_{\rm cap} = \frac{\kappa}{a^2 C_a}, \tag{29}$$

where B_o is the Bond number and C_a is the capillary number.

As an example test case, we consider the subsurface movement of supercritical CO_2 for carbon sequestration. At a 2 Km depth, the system will be roughly at 340K and under 20 MPa of pressure [36]. Under these conditions, $\Delta\rho \approx 0.35 \text{g/cm}^3$ and $\gamma \approx 27 \text{mN/m}$ [37]. The viscosity of the supercritical carbon dioxide is $\mu = 0.048$ mPa s [38]. A likely injection scenario involves a flux of approximately 3 Mton of carbon dioxide per year, which is equivalent to about 100 liters/second [36]. At a distance of only 10 meters from the injection point, this corresponds to a fluid velocity of approximately $V = 3 \times 10^{-4}$ cm/s, for a material with porosity of 0.3. The ratio κ/a^2 is typically small, approximately 10^{-3} [1].

For this model system, the corresponding capillary number is $C_a = \mu v/\gamma = 5 \times 10^{-9}$. For pores of size 0.1 mm, the Bond number is $B_o = \Delta\rho g a^2/\gamma = 1.3 \times 10^{-3}$. The resulting dimensionless cutoffs are $L_{\rm grav} \approx 10^3$, and $L_{\rm cap} \approx 10^6$, corresponding to 10 cm and 100 m, respectively. For systems larger than these cutoffs, buoyant and viscous effects must be included in the invasion percolation algorithm by including spatial gradients in the bond invasion preferences [26, 35, 39]. Note that the values used here are not meant to predict geological carbon sequestration conditions with high accuracy, but are meant to illustrate the critical length scales and show that omitting viscous and buoyant effects is reasonable over the size scales of our simulations.

V. CONCLUSION

In summary, we have shown that complex geometric boundary conditions emergent in two-phase porous flow have profound effects on the bounded reaction-diffusion processes. We

have shown that the chemistry at each point in the reactive phase is determined by the full distribution of first-passage diffusion times, and scalar geometric measures are insufficient to accurately predict concentrations due to the reactions. We have studied the scaling behavior of the moments of these distributions both in simulation and in an idealized spherical bubble approximation. The analytic approximation is successful in two dimensions in that it accurately predicts scaling laws describing the first-passage time distributions, and therefore can accurately predict concentrations. However, the simple spherical approximation fails to account for the convoluted shapes of bubbles in three dimensions. The existence of the power-law scaling implies that shapes and structures exist of all length scales permitted by the system size. Therefore, averages taken over the system, such as the average chemical concentration, depend upon that arbitrary choice of system size. This complication must be accounted for in any accurate coarse-graining of the system.

Acknowledgments

We would like to thank the reviewers for their helpful suggestions. This material is based upon work supported as part of the Center for Nanoscale Control of Geologic CO_2, an Energy Frontier Research Center funded by the U.S. Department of Energy, Office of Science, Office of Basic Energy Sciences under Award Number: DE-AC02-05CH11231, subcontract 6896518.

---

[1] D. Wilkinson, Journal of Physics A: Mathematical and General **16**, 3365 (1983).

[2] M. Dias and D. Wilkinson, Journal of Physics A: Mathematical and **19**, 3131 (1986), URL `http://iopscience.iop.org/0305-4470/19/15/034`.

[3] D. Stauffer, Physics reports (1979), URL `http://www.sciencedirect.com/science/article/pii/0370157379900607`.

[4] A. Kumar, M. Noh, G. Pope, K. Sepehrnoori, S. Bryant, and L. Lake, Proceedings of SPE/DOE Symposium on Improved Oil Recovery (2004), URL `http://www.spe.org/elibrary/servlet/spepreview?id=00089343`.

[5] Y. Ghomian, G. A. Pope, and K. Sepehrnoori, Energy **33**, 1055 (2008), ISSN 03605442, URL

http://linkinghub.elsevier.com/retrieve/pii/S0360544208000509.

[6] P. Scharlin, *Carbon dioxide in water and aqueous electrolyte solutions* (Oxford University Press, Oxford, 1996), URL http://scholar.google.com/scholar?hl=en\&btnG=Search\&q=intitle:Carbon+dioxide+in+water+and+aqueous+electrolyte+solutions\#6.

[7] T. Wellman, R. Grigg, B. McPherson, R. Svec, and C. Peter, Internation Symposium on Oilfield Chemistry **15**, 379 (2003), URL http://www.onepetro.org/mslib/servlet/onepetropreview?id=00080228.

[8] A. Ahmadi, M. Quintard, and S. Whitaker, Advances in water resources **22**, 59 (1998), URL http://www.sciencedirect.com/science/article/pii/S0309170897000328.

[9] C. Steefel and P. C. Lichtner, Journal of Hydrology **209**, 186 (1998), ISSN 00221694, URL http://linkinghub.elsevier.com/retrieve/pii/S0022169498001462http://www.sciencedirect.com/science/article/pii/S0022169498001462.

[10] L. R. Kump, S. L. Brantley, and M. A. Arthur, Annual Review of Earth and Planetary Sciences **28**, 611 (2000), URL http://arjournals.annualreviews.org/doi/abs/10.1146/annurev.earth.28.1.611.

[11] C. Steefel, D. DePaolo, and P. Lichtner, Earth and Planetary Science Letters (2005), URL http://www.sciencedirect.com/science/article/pii/S0012821X05005984.

[12] P. Lichtner and Q. Kang, Water Resources Research (2007), URL http://www.agu.org/pubs/crossref/2007/2006WR005664.shtml.

[13] A. Navarre-Sitchler and S. Brantley, Earth and Planetary Science Letters **261**, 321 (2007), ISSN 0012821X, URL http://linkinghub.elsevier.com/retrieve/pii/S0012821X07004426.

[14] R. C. Fletcher and S. L. Brantley, American Journal of Science **310**, 131 (2010), ISSN 0002-9599, URL http://www.ajsonline.org/cgi/doi/10.2475/03.2010.01.

[15] M. Dentz, P. Gouze, and J. Carrera, Journal of contaminant hydrology **120-121**, 222 (2011), ISSN 1873-6009, URL http://www.ncbi.nlm.nih.gov/pubmed/20609494.

[16] M. Dentz, T. L. Borgne, and A. Englert, Journal of Contaminant (2011), URL http://www.sciencedirect.com/science/article/pii/S0169772210000495.

[17] R. Zeebe, *CO2 in seawater: equilibrium, kinetics, isotopes* (Elsevier, Amsterdam, 2001), URL http://books.google.com/books?hl=en\&lr=\&id=VrumU3XvQ-gC\&oi=fnd\&pg=PP2\&dq=Co2+in+Seawater:+Equilibrium,+Kinetics,+Isotopes\

&ots=0lLG_eWi3-\&sig=JKjFZxaOyPnqYZGdwH1kYp1loMk.

[18] M. Lebedeva, R. Fletcher, V. Balashov, and S. Brantley, Chemical Geology **244**, 624 (2007), ISSN 00092541, URL http://linkinghub.elsevier.com/retrieve/pii/S0009254107003294.

[19] M. Lebedeva, R. Fletcher, and S. Brantley, Earth Surface Processes and Landforms **524**, n/a (2010), ISSN 01979337, URL http://doi.wiley.com/10.1002/esp.1954.

[20] C. Steefel and A. Lasaga, American Journal of Science **294**, 529 (1994).

[21] C. I. Steefel and K. Maher, Reviews in Mineralogy and Geochemistry **70**, 485 (2009), URL http://rimg.geoscienceworld.org.

[22] M. Blunt and M. King, Physical Review A (1992), URL http://pra.aps.org/abstract/PRA/v46/i12/p7680_1.

[23] G. N. Constantinides and A. C. Payatakes, Transport in porous media **38**, 291 (2000), URL http://www.springerlink.com/index/V119106327570257.pdf.

[24] S. J. Wettstein, F. K. Wittel, N. A. M. Araújo, B. Lanyon, and H. J. Herrmann, Physica A **391**, 264 (2012), ISSN 03784371, URL http://linkinghub.elsevier.com/retrieve/pii/S0378437111005760.

[25] J. Ross and M. Vlad, Annu. Rev. Phys. Chem pp. 51–78 (1999), URL http://scholar.google.com/scholar?hl=en\&btnG=Search\&q=intitle:Nonlinear+kinetics+and+new+approaches+to+complex+reaction+mechanisms\#2.

[26] P. Meakin, A. Birovljev, V. Frette, and J. Feder, Physica A: Statistical **191**, 227 (1992), URL http://www.sciencedirect.com/science/article/pii/037843719290532U.

[27] A. Birovljev, G. Wagner, P. Meakin, and J. Feder, Physical Review E **51** (1995), URL http://pre.aps.org/abstract/PRE/v51/i6/p5911_1.

[28] P. Meakin, G. Wagner, A. Vedvik, H. Amundsen, J. Feder, and T. Jossang, Marine and Petroleum Geology **17**, 777 (2000), ISSN 02648172, URL http://linkinghub.elsevier.com/retrieve/pii/S0264817299000690.

[29] P. Levitz, D. Grebenkov, M. Zinsmeister, K. Kolwankar, and B. Sapoval, Physical Review Letters **96**, 1 (2006), ISSN 0031-9007, URL http://link.aps.org/doi/10.1103/PhysRevLett.96.180601.

[30] A. Lowan, Bull. Amer. Math. Soc **24**, 62 (1938), URL http://www.ams.org/journals/bull/1938-44-02/S0002-9904-1938-06707-9/S0002-9904-1938-06707-9.pdf.

[31] H. C. Berg, *Random walks in biology* (Princeton University Press, Princeton, 1993).

[32] M. Armstrong, *Basic topology* (Springer-Verlag, New York, 2010), ISBN 0-387-90839-0, URL http://en.scientificcommons.org/9239148.

[33] L. Paterson, A. Sheppard, and M. Knackstedt, Physical Review E **66**, 1 (2002), ISSN 1063-651X, URL http://link.aps.org/doi/10.1103/PhysRevE.66.056122.

[34] D. Wilkinson, Physical Review A **30** (1984), URL http://pra.aps.org/abstract/PRA/v34/i2/p1380_1http://pra.aps.org/abstract/PRA/v30/i1/p520_1.

[35] V. Frette, J. Feder, T. Jossang, and P. Meakin, Physical review letters **68**, 3164 (1992), URL http://link.aps.org/doi/10.1103/PhysRevLett.68.3164.

[36] C. Ehlig-Economides and M. J. Economides, Journal of Petroleum Science and Engineering **70**, 123 (2010), ISSN 09204105, URL http://linkinghub.elsevier.com/retrieve/pii/S0920410509002368.

[37] P. Chiquet, J.-L. Daridon, D. Broseta, and S. Thibeau, Energy Conversion and Management **48**, 736 (2007), ISSN 01968904, URL http://linkinghub.elsevier.com/retrieve/pii/S0196890406002913.

[38] A. Fenghour, W. A. Wakeham, and V. Vesovic, Journal of Physical and Chemical Reference Data **27**, 31 (1998), ISSN 00472689, URL http://link.aip.org/link/JPCRBU/v27/i1/p31/s1\&Agg=doi.

[39] M. Chaouche, N. Rakotomalala, D. Salin, and B. Xu, Physical Review E **49** (1994), URL http://pre.aps.org/abstract/PRE/v49/i5/p4133_1.